Stellar Surface Magneto-convection as a Source of Astrophysical Noise. II. Center-to-limb Parameterization of Absorption Line Profiles and Comparison to Observations

The Astrophysical Journal, 866:55 (14pp), 2018 October 10 https://doi.org/10.3847/1538-4357/aaddfc

Stellar Surface Magneto-convection as a Source of Astrophysical Noise. II. Center-to-limb Parameterization of Absorption Line Profiles and Comparison to Observations

H. M. Cegla[1,2,8], C. A. Watson[2], S. Shelyag[3], W. J. Chaplin[4,5], G. R. Davies[4,5], M. Mathioudakis[2], M. L. Palumbo III[6], S. H. Saar[7], and R. D. Haywood[7,9]

[1] Observatoire de Genève, Université de Genève, 51 Chemin des Maillettes, CH-1290 Versoix, Switzerland; h.cegla@unige.ch
[2] Astrophysics Research Centre, School of Mathematics & Physics, Queen's University Belfast, University Road, Belfast BT7 1NN, UK
[3] Department of Mathematics, Physics and Electrical Engineering, Northumbria University, Newcastle upon Tyne, NE1 8ST, UK
[4] School of Physics and Astronomy, University of Birmingham, Edgbaston, Birmingham B15 2TT, UK
[5] Stellar Astrophysics Centre, Department of Physics and Astronomy, Aarhus University, Ny Munkegade 120, DK-8000 Aarhus C, Denmark
[6] Department of Physics and Astronomy, University of North Carolina at Chapel Hill, 120 E Cameron Ave, Chapel Hill, NC 27514, USA
[7] Harvard-Smithsonian Center for Astrophysics, 60 Garden Street, Cambridge, MA 02138, USA
Received 2018 June 6; revised 2018 August 27; accepted 2018 August 28; published 2018 October 11

Abstract

Manifestations of stellar activity (such as star-spots, plage/faculae, and convective flows) are well-known to induce spectroscopic signals often referred to as astrophysical noise by exoplanet hunters. For example, setting an ultimate goal of detecting true Earth analogs demands reaching radial velocity (RV) precisions of $\sim$9 cm s^{-1}. While this is becoming technically feasible with the latest generation of highly stabilized spectrographs, it is astrophysical noise that sets the true fundamental barrier on attainable RV precisions. In this paper, we parameterize the impact of solar surface magneto-convection on absorption line profiles, and extend the analysis from the solar disk center (Paper I) to the solar limb. Off disk-center, the plasma flows orthogonal to the granule tops begin to lie along the line of sight, and those parallel to the granule tops are no longer completely aligned with the observer. Moreover, the granulation is corrugated and the granules can block other granules, as well as the intergranular lane components. Overall, the visible plasma flows and geometry of the corrugated surface significantly impact the resultant line profiles and induce center-to-limb variations in shape and net position. We detail these herein, and compare to various solar observations. We find our granulation parameterization can recreate realistic line profiles and induced radial velocity shifts, across the stellar disk, indicative of both those found in computationally heavy radiative 3D magnetohydrodynamical simulations and empirical solar observations.

Key words: line: profiles – planets and satellites: detection – stars: activity – stars: low-mass – Sun: granulation – techniques: radial velocities

1. Introduction

There are many phenomena on the surfaces of potentially planet-hosting, low-mass, main sequence stars that prevent them from being perfect, homogeneous spheres. For example, such stars experience stellar surface magneto-convection (granulation), oscillations, flares, dark starspots, and bright networks of faculae/plage with regions of (magnetically) suppressed convection. In addition, they also exhibit magnetic activity cycles that drive quasi-periodic variations in the properties of such features, such as their distributions, sizes, filling factors, and lifetimes. From a spectroscopic point of view, these phenomena can alter the observed stellar line profiles, and in turn may be mistakenly interpreted as wholesale Doppler shifts—referred to as astrophysical noise or stellar "jitter." The level of astrophysical noise on a typical exoplanet host may range from 10 s of cm s^{-1} to 100 s of m s^{-1} (Saar & Donahue 1997; Schrijver & Zwaan 2000); as such, these spurious signals from the star completely swamp the 9 cm s^{-1} Doppler-reflex motion induced by a true Earth analog (and can even mimic some planets, e.g., see Robertson et al. (2015)). This is particularly troubling, as our best hope for the confirmation of an Earth twin is from the spectroscopic follow-up of small planet candidates found in photometric surveys (e.g., *Kepler*/*K2*, *TESS*, and *PLATO*). Moreover, as spectrographs capable of 10 cm s^{-1} precision start to come online (e.g., ESPRESSO has recently seen first light[10]), the impact of astrophysical noise will increasingly represent the fundamental limit to the confirmation and characterization of exoplanets—and it is this aspect, rather than instrumental capabilities, that will be critical in the search and confirmation of Earth analogs.

Even "quiet" non-active stars exhibit oscillations and stellar surface magneto-convection/granulation. In particular, pressure (p-) modes give rise to periodic perturbations of the stars, and hence induce Doppler shifts, with dominant timescales on the order of several minutes for Sun-like stars (Christensen-Dalsgaard 2002, and references therein). Granulation induces radial velocity (RV) shifts by creating asymmetries in the line profiles from the combination of hot, uprising, blueshifted granules and cool, redshifted, sinking, intergranular lanes. This can result in a net convective blueshift because the granules are brighter and cover more surface area (Stein 2012, and references therein). The timescales for granulation are similar to the p-modes, because it is the turbulent motions in the convective envelope that drive the acoustic oscillations, and both are tied to the stellar surface gravity (Kallinger et al. 2014, and references therein). However, because the granules tend to appear and disappear in the same

[8] CHEOPS Fellow, SNSF NCCR-PlanetS.
[9] NASA Sagan Fellow.
[10] https://www.eso.org/public/news/eso1739/

locations, long exposure times do not completely average out the granulation impact. The current mitigation technique for this noise is to simply "beat it down" by adjusting the number of observations and exposure times (Dumusque et al. 2011); however, this is extremely costly and may reach a fundamental noise floor. Moreover, oscillations may be easier to "beat down" than granulation, despite their similar timescales, because they produce narrowband signals (i.e., higher quality factor, with lower relative damping) that can readily be filtered, while the granulation has a pink-noise-like signature spread in frequency. For example, Chaplin et al. (2018) demonstrate that solar oscillations can be averaged out to $\lesssim$10 cm s^{-1} with an exposure time of ∼5.4 minutes, while Meunier et al. (2015) argue that it would take more than one night to average the granulation signal to the 10 cm s^{-1} level. Consequently, in this series of papers, we explore the impact of stellar surface magneto-convection as a source of astrophysical noise.

In Paper I (Cegla et al. 2013), we outlined our technique for characterizing photospheric magneto-convection at disk center. The backbone of this characterization is a state-of-the-art 3D magnetohydrodynamic (MHD) solar simulation, coupled with detailed wavelength-dependent radiative transfer. Due to the time-intensive nature of detailed radiative diagnostics, producing enough realistic granulation patterns to cover an entire stellar disk with this method is not feasible. As a result, we developed a multi-component parameterization of granulation at disk center from a short time series of simulations, and have shown that we can reconstruct the line profile asymmetries and RV shifts due to the photospheric convective motions found in the MHD-based simulations. The parameterization is composed of absorption line profiles calculated for granules, magnetic intergranular lanes, non-magnetic intergranular lanes, and magnetic bright points (MBPs) at disk center. These components were constructed by averaging Fe I 6302 Å magnetically sensitive absorption line profiles output from detailed radiative transport calculations of the solar photosphere.

In this paper, we extend the multi-component parameterization of stellar surface magneto-convection from disk center (Paper I) toward the stellar limb. In a forthcoming publication (Paper III), this parameterization will be used to create new absorption line profiles that represent realistic granulation patterns and create Sun-as-a-star model observations; these artificially noisy model stars will then be used to test astrophysical noise reduction techniques. For a comprehensive overview of general granulation properties, such as granule areas, intensities, lifetimes, and flow characteristics etc., we direct the reader to the HD and MHD simulations of Beeck et al. (2013a, 2013b, 2015a, 2015b) for FGKM stars. Here, we specifically focus on parameterizing solar simulations, with an average magnetic field of 200 G, in order to understand the center-to-limb behavior and enable the future generation of realistic granulation line profiles.

In Section 2, we show how the average granulation line profiles from the simulation snapshots change as a function of center-to-limb angle, and in Section 3 we break this down into how each of the four granulation components change. We explore the accuracy of the parameterization across the stellar disk in Section 4, and compare to observations in Section 5. Finally, we conclude in Section 6. It is important to note that the underlying MHD simulation and radiative transport code have undergone minor changes since Paper I (see Section 2 for details).

2. Center-to-limb Variations in the Average Absorption Line Profiles

2.1. Simulation Details

Similar to Paper I, we use the MURaM code to produce 3D MHD solar surface simulations (Vögler et al. 2005). The numerical domain has a physical size of 12 × 12 Mm^2 in the horizontal direction and 2.0 Mm in the vertical direction, and is resolved by 480 × 480 × 200 grid cells. Note that the simulation box has increased in depth since Paper I, in order to circumvent any potential issues with boundary conditions, and the equation of state has also been upgraded to OPAL (Rogers et al. 1996; Rogers & Nayfonov 2002). The simulation box is inclined in 2° steps from disk center to 80°. Inclinations beyond 80° were computationally unfeasible due to the $1/\cos(i)$ dependency, requiring a significantly longer ray-path. Nonetheless, we note that this corresponds to ∼0.91 times the solar radius, and as the small annulus beyond this is heavily limb-darkened, it contributes less than 5% to the total integrated flux.

Again, we have introduced a uniform vertical 200 G magnetic field, and this time we produced a sequence of 201 snapshots. Note that the MHD simulation did not have exactly even time steps. We have tried to select snapshots with a cadence as close to 30 s as possible, but nearly a third of the snapshots (that are randomly distributed in the series) have a sampling closer to 15 s. This sequence covers approximately 100 minutes of physical time or ∼10–25 granular lifetimes. See Paper I for more details. We have used the 1D radiative transport code NICOLE (Socas-Navarro 2015; Socas-Navarro et al. 2015), in conjunction with the MHD simulation, to synthesize the Fe I 6302 Å magnetically sensitive absorption line in local thermodynamic equilibrium (LTE). Similar to Paper I, we focus only on the Stokes I component, and resolve a ±0.3 Å region with 400 points. Note that, with NICOLE, we have used updated opacities relative to Paper I. The changes in the MURaM code, and to NICOLE for the line synthesis, were motivated by comparisons with observations (see Section 5 for more details). The technical details on the absorption line profile calculations for inclined models and simulated spectro-polarimetry off the solar disk center are provided in Shelyag & Przybylski (2014) and Shelyag (2015).

2.2. Center-to-limb Variations

Toward the stellar limb, the absorption line profiles are subject both to limb darkening and the fact that the granulation makes the surface appear corrugated; this is illustrated in Figure 1, where the continuum intensity and line-of-sight (LOS) velocities of one snapshot are shown for disk center and near the limb (0° and 60°)—note that blueshifts are denoted by negative velocities and redshifts by positive velocities. An apt analogy for the corrugated surface is to think of the granules as hills and the intergranular lanes as valleys (Dravins 2008). As the simulation is inclined, some of the granular "hills" obstruct the intergranular lane "valleys," the sides of the granular walls become visible, and parts of the granule tops can be obscured. Moreover, toward the stellar limb, plasma flows that were perpendicular to the LOS at disk center are no longer completely orthogonal to the viewer and thus have non-zero RVs. Additionally, the purely vertical flows at disk center are now inclined with respect to the LOS, and the observed RVs decrease in magnitude as a function of the projected area.

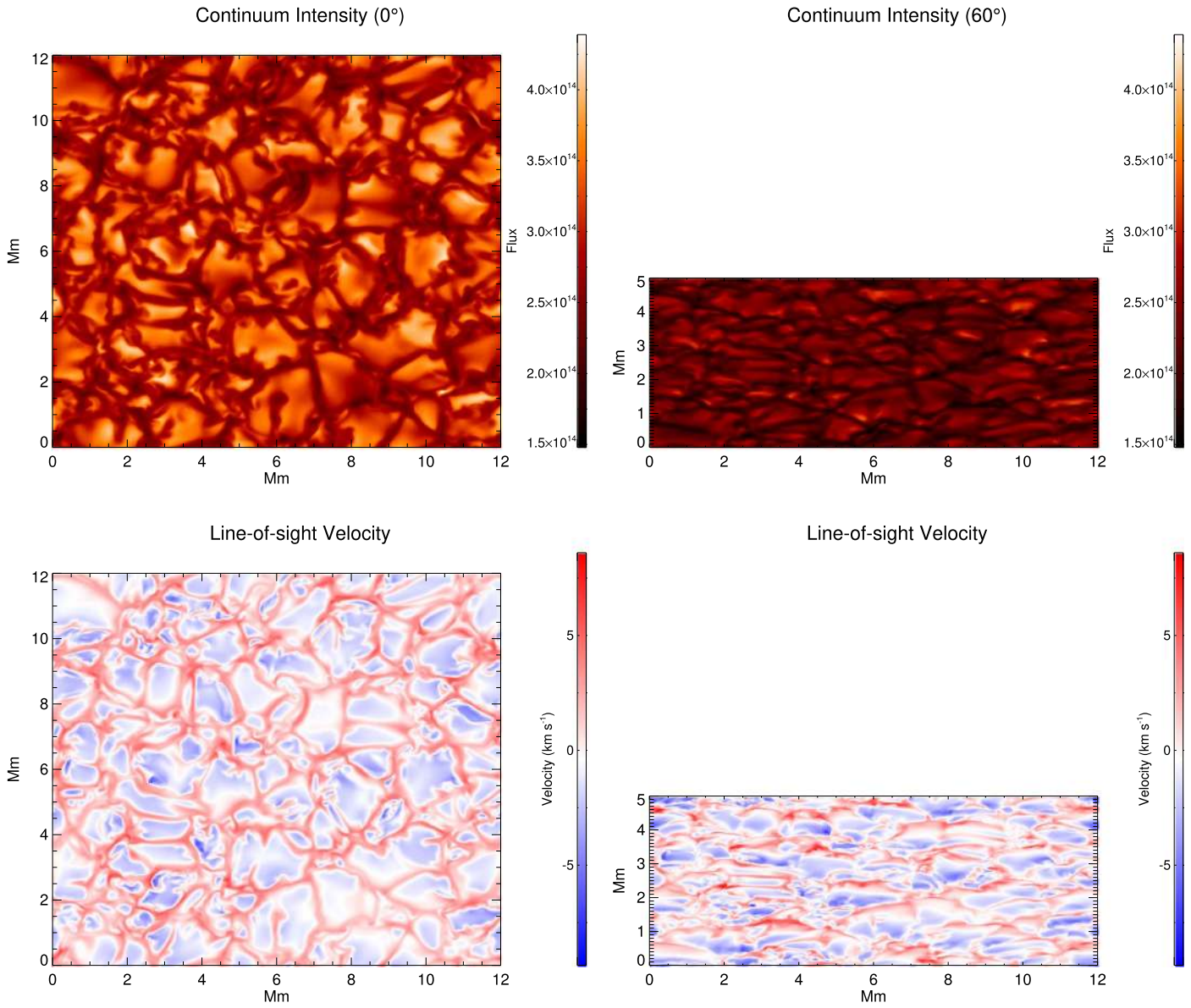

Figure 1. Continuum intensities (top) and line-of-sight velocities (bottom) for one simulation snapshot at two different stellar disk center-to-limb angles: 0° (left) and 60° (right). Negative and positive velocities denote blueshifts and redshifts, respectively.

Toward the limb, only the near-edges of the granules have high blueshifts, as this is where the plasma is starting to flow into the intergranular lane and hence lies more inline with our LOS. The remainder of the granule tops point away from the observer, and plasma flows that were once seen as coming toward the observer now begin to point away, resulting in a decrease in blueshift of the granules as whole. The opposite effect is seen in the intergranular lanes, where some of the downward-flowing material is now flowing toward the observer as the tiles are inclined. It is also possible to see the intergranular lanes underneath some of the smaller granules. See Section 3.2 for more details on the responses of individual granulation components. As a consequence of this corrugation, we see differences in line shape, line center, and filling factor for each of the granulation components as a function of limb angle (discussed in the Section 3); this directly results in the average granulation RV also changing as a function of limb angle.

Of particular significance is the center-to-limb variation (CLV) of the net convective velocities. From solar observations, we can expect a CLV on the 100 m s^{-1} level, becoming more redshifted toward the stellar limb (Dravins 1982); this is because plasma flows moving away from the observer are more often seen in front of the hotter (i.e., brighter) plasma above the intergranular lanes, and the flows toward the observer are increasingly blocked from view by granules located in the forefront of the LOS (see Balthasar 1985; Asplund et al. 2000, and references therein). To investigate this relative variation in our simulations, we use the approach outlined in Paper I to compute the RVs: the average line profile from each individual snapshot in the time series is cross-correlated against an arbitrarily chosen template profile. The template was created from the parameterized reconstruction described in Section 4, but merely serves as a reference point. The same disk center template is used for all limb angles. As such, these net RVs are relative to disk center and are not absolute. The results from individual snapshots are shown as red lines, and the average over the time series is shown in the form of

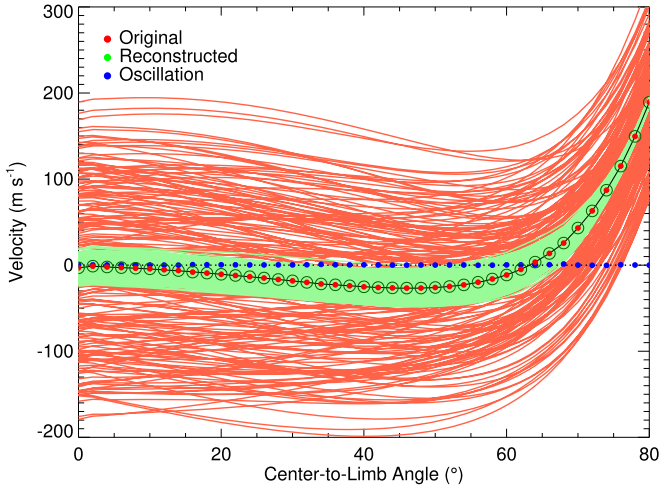

Figure 2. Net RVs relative to disk center for both individual snapshots (lines) and averages over the time series (points); original profile results are in red, connected by a solid black line, and the reconstructed (granulation-only) profiles are in green (see Sections 3 and 4 for details). Scatter from individual profiles is due to p-modes and granular evolution (reconstruction only includes granular effects). Also plotted are the oscillation RVs averaged over the entire series (blue points), and a black dotted line at 0 m s^{-1} to guide the eye.

red points in Figure 2. The pronounced variation among individual snapshots originates from the RV shifts introduced from p-mode oscillations that are naturally excited by the convection in the simulation box, which are approximately a factor of ten larger in amplitude than the granulation induced shifts (shown in green—derived from the granulation parameterization in Section 3 and the subsequent line profile reconstruction in Section 4). As discussed in Section 3.1, these oscillations can largely be averaged out over the time series, and hence appear near 0 in Figure 2 (blue dots); in empirical observations, the p-modes may also be averaged to a root-mean-square $\lesssim$10 cm s^{-1} with an exposure time of 5.4 minutes for the Sun (Chaplin et al. 2018). Consequently, we focus on the nature of the time-averaged net RV variation over the stellar disk.

From our simulations, we find a net redshift near the limb of $\sim$200 m s^{-1}, relative to disk center—in line with what we expect from solar observations. Part of this net RV CLV is due to projected area effects. However, the change in net RVs is not only larger in magnitude than the cos(i) term from the projected area, but also deviates from this effect because the stellar surface is corrugated. From Figure 2, we see an initial increase in the net blueshift, which is likely due to increased contributions from velocity flows on the granule tops that have an LOS component away from disk center. This increase in blueshift continues until a limb angle of 46° ($\mu \approx 0.7$, where $\mu = \cos(\theta)$). Then, near the limb (>60°), we see a rapid increase in the relative redshift, owing to the aforementioned velocity flows seen in the hot/bright plasma above the intergranular lanes. The net impact seen here is further broken down into the impact from individual granulation components in Section 3.

2.3. Oscillations

The magneto-convection in the simulation box naturally excites p-modes and f-modes (surface gravity flows), as happens on the real Sun. We note that, while f-modes have been detected at low frequencies in high-resolution data on the Sun, they have very low amplitudes and cannot be detected in Sun-as-a-star data. The various modes both constructively and destructively interfere with one another to induce oscillatory variations in the line profiles. Because the oscillations are not only stochastically excited but are also intrinsically damped by the convection, the signal dephases on a timescale commensurate with the damping time for each mode. The hypothesis from Paper I was that the oscillations only induced wholesale Doppler shifts and did not significantly change the line profile shape (Gray 2005), and the vertical scatter within the individual line profiles was naively attributed solely to granulation. However, further inspection of the power spectra densities (PSDs), calculated via fast Fourier transforms, show clear periodicities in both the RVs and line shape parameters (e.g., line depth, width, and equivalent width etc.) in the classic "five-minute solar oscillation" range ($\sim$3 mHz). Moreover, the p-mode induced[11] Doppler shifts and line shape variations are up to an order of magnitude larger than those induced from convection in our simulation box (e.g., compare RVs in Figures 3 and 10). Note that a decrease in numerical plasma viscosity in the MHD simulation from Paper I means the oscillation never completely dampens out in this time series.

From solar observations, we expect the amplitude of the p-modes to decrease in amplitude toward the stellar limb (Schmidt et al. 1999). This is due to two contributing factors: near the limb, we see a combination of vertical and horizontal velocity flows, and the inclined LOS means we are viewing areas that are physically higher in the solar atmosphere. In Figure 3, we show both the decrease in amplitude of the p-mode oscillation as a function of limb angle, and the decrease in power as seen in the PSD. At 80° ($\mu \approx 0.17$), the p-mode amplitudes are barely visible and the power is decreased by nearly 90% compared to disk center. These findings are in agreement with Löhner-Böttcher et al. (2018) and their recent high-precision solar observations with the LARS spectrograph.

3. The Four-component Model: Across the Stellar Disk

Here, we extend the multi-component parameterization of solar surface magneto-convection from disk center in Paper I toward the stellar limb, in steps of 2°, up to an angle of 80° ($\mu \approx 0.17$). The individual line profiles that correspond to each pixel are still separated into four different granulation components, using continuum intensity and magnetic field cuts. We use the same cuts as Paper I: 0.9 times the average continuum intensity (at each limb angle) of a randomly chosen snapshot and 1 kG times cosine of the limb angle (note that, although the average magnetic field of the simulation is 200 G, once this is advected into the intergranular lanes by the granules, regions within a given snapshot can easily reach values >1 kG). The magnetic field cut away from disk center is not perfect, as it assumes that the fields are purely radial from the center of the star, which is not strictly true; however, the contribution from non-radial magnetic flux is comparatively small, so this cut should be reasonable to separate magnetic and non-magnetic components. All snapshots are scaled to the projected area at each limb angle; for the magnetic field, we operate on the LOS along a region of constant temperature corresponding to the stellar surface (5800 K). As such, we maintain the same four categories used in Paper I: granules (bright/non-magnetic), MBPs, and both magnetic and non-magnetic intergranular lanes.

[11] Identified by their peak periodicities.

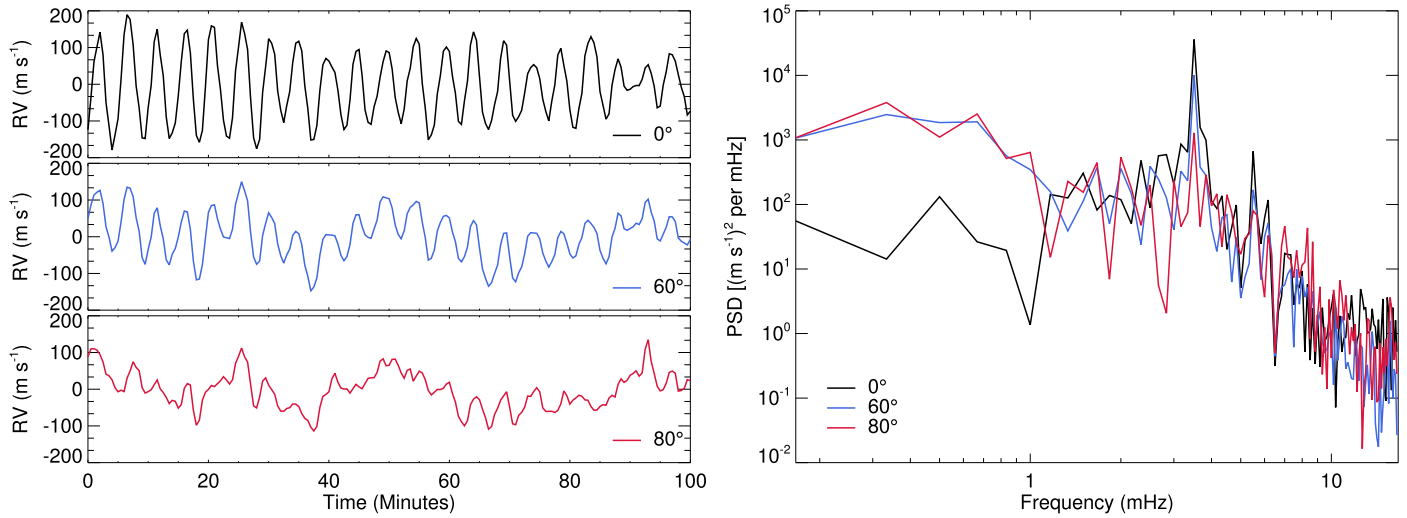

Figure 3. Original RVs from the average line profiles from each snapshot over the time series (left) and their corresponding power spectra (right) for limb angles 0°, 60°, and 80°; these include contributions from both p-mode oscillations and granulation.

The four granulation components are shown in Figure 4 for center-to-limb angles: 0°, 20°, 40°, and 60°; average profiles over the time series are shown in thick, dark lines and components from individual snapshots are shown in lighter, narrower lines.[12] Note that each individual profile has been shifted in velocity to remove some of the effects from the oscillations, as further discussed in Section 3.1 (visually, this is a small effect, with shifts <0.0042 Å); most of the remaining (horizontal and vertical) scatter is due to imperfect removal of the oscillation signal.

3.1. Removing the Oscillations

As mentioned in Section 2.3, the oscillations induce variations in both the line profile centers and shapes. At present, we operate under the hypothesis that, over the stellar disk, these oscillation-induced variations will average out over an appropriately chosen exposure time, but that the granulation variations will still be present. This hypothesis is based on the fact that the granules, as observed on the Sun and in the simulations, tend to appear and disappear in the same locations, making the granulation noise more correlated over time than that from the p-modes. Testing the extent to which this hypothesis stands will be the subject of a future study. As such, herein we seek to remove the impact of the oscillations on our granulation parameterization; this is especially important given that the oscillation-induced variability is orders of magnitude larger than that from the granulation in our simulation box.

To remove the oscillations, we follow the procedure outlined in Paper I, where each component profile is shifted by its mean bisector to a rest velocity determined by the respective average bisector position over the time-series. Once the profiles have been shifted, the respective individual components are averaged together to create four granulation component line profiles. Shifting the profiles before creating the final time-average helps prevent the component profiles from being skewed by oscillation-induced broadening (depending on the line depth, the average component profiles were $\sim$1–10 m s^{-1} wider before removing the oscillation—with the largest differences at the tops of the profiles). The line shape parameters also vary due to the oscillations; this can been seen in the remaining scatter of the individual profiles about their means in Figure 4. However, if the bulk of the movement in the wavelength/velocity domain has been removed, then the shape changes should largely average out over the time series without significant skewing of the profile shapes.

3.2. Center-to-limb Variations

Over the stellar disk, all four components experience changes in line profile shape and net velocity. The behavior between the magnetic and non-magnetic components differ slightly due to the Zeeman splitting in the magnetic components. The non-magnetic components experience a continual decrease in continuum intensity (from limb darkening), shown in Figure 5 (and also visible in Figure 1); these profiles also decrease in line depth/contrast, as well as increase in line width. The changes in line width/depth are due to increasing contributions from plasma flows that were horizontal at disk center. On the other hand, the magnetic components initially become narrower and deeper once the LOS moves away from disk center. This is likely because the LOS traverses inclined magnetic flux tubes and therefore does not penetrate as much magnetic flux as when at disk center; this results in a decrease of the Zeeman splitting in the line profiles (Shelyag 2015). Moreover, near the limb, we view regions higher in the photosphere, and therefore these components may also experience a decrease in their thermal broadening. The MBP components also do not decrease significantly in continuum intensity until closer to the limb (see Figure 5); this is likely because they change from point-like structures within the intergranular lanes at disk center (that are bright due to enhanced continuum intensity and decreased radiation absorption) to also include bright regions (known as faculae) on the granular walls at higher inclinations. While the granule itself is non-magnetic, as the granulation snapshot is inclined, high magnetic field concentrations in the intergranular lanes decrease the opacity and allow the LOS to reach the granular wall. Such regions then have high brightnesses due to the high temperature of the granule, yet a high magnetic field measurement due to the LOS traversing

[12] The overall shapes of these components (at disk center) can be compared with Figure 8 in Beeck et al. (2015b), where the authors select profiles from four regions of different magnetic field strength and brightness—however, we note that these authors simulate a K0V star with average magnetic field of 500 G, and synthesize the Fe I 6173 Å line.

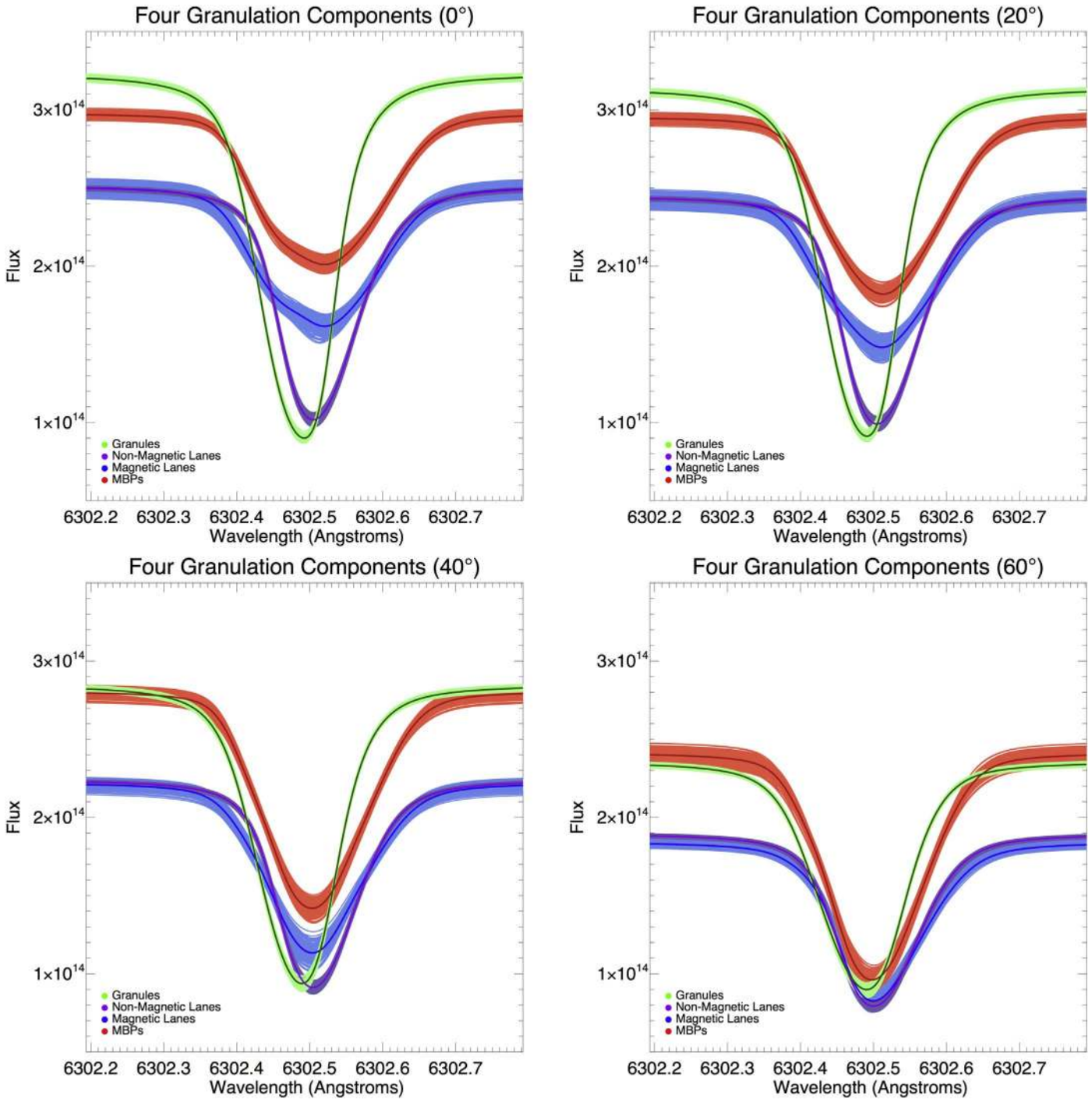

Figure 4. Average (thick) and individual (thin) line profiles from the four different contributions to granulation used in the parameterization: granules (green), MBPs (red), and magnetic (blue) and non-magnetic (purple) intergranular lanes, for four different stellar disk center-to-limb angles. Flux is measured in units of erg s^{-1} cm^{-2} sr^{-1} $Å^{-1}$.

regions of high magnetic field within the relatively transparent intergranular lane. Although these regions are better known as faculae and do not necessarily have point-like surface areas, we include them in the MBP category across the stellar disk because they are both magnetic and bright. As a result, the decrease in brightness of the MBPs as the simulations are inclined is partially compensated by the appearance of the new MBPs on the granular walls, until $\sim$40°.

The plasma flows orthogonal to the granule tops also change the net position of the components, resulting in the granule profiles redshifting and the intergranular lane profiles blueshifting relative to disk center. This is explicitly shown in Figure 6, where the RVs were calculated in the same manner as Section 2.2, but replacing the full line profile in the template with the respective component profiles; it is also visible in the LOS velocity maps shown in bottom of Figure 1. Some of the vertical LOS velocities at disk center begin to lie more orthogonal to our LOS as we view granulation toward the limb and they consequently decrease in magnitude. In particular, only the near edges of the granules have high blueshifts, as

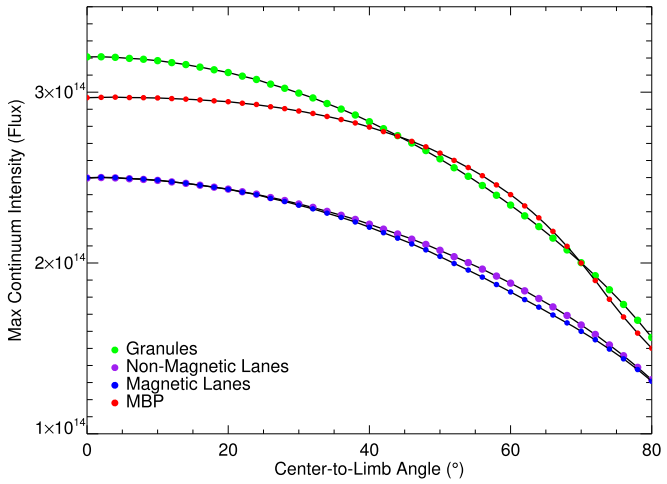

Figure 5. Maximum continuum intensity of the four granulation components as a function of limb angle; note that the magnetic and non-magnetic intergranular lanes values are nearly identical. The initial near-constant brightness of the MBP component may be due to inclusion of faculae.

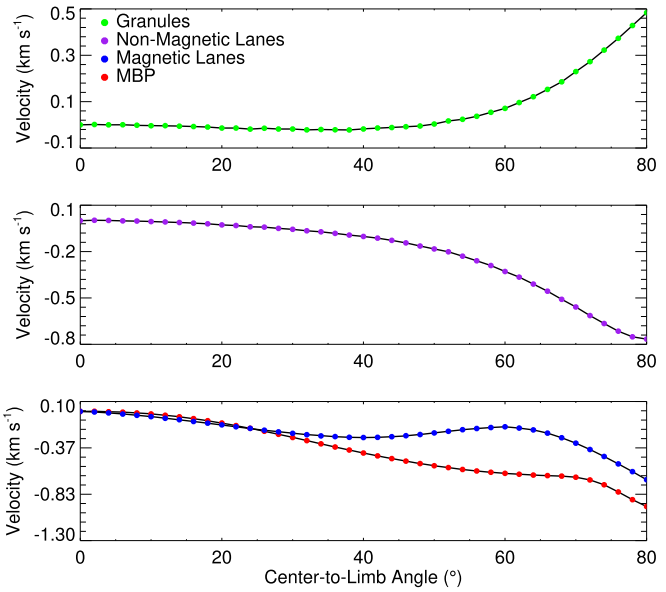

Figure 6. RV of the four granulation components relative to disk center as a function of limb angle.

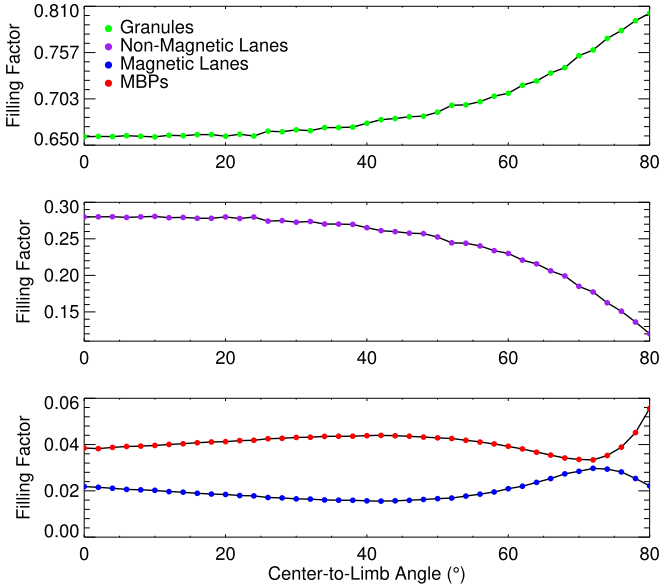

Figure 7. Filling factors for the four granulation components as a function of limb angle.

seen in Figure 1, because this is where the plasma has begun to flow into the intergranular lane and now lies more inline with our LOS; the remainder of the top of the granule begins to point away from the observer. The opposite effect is seen in the intergranular lanes, where some of the downward-flowing material is now flowing toward the observer as the tiles are inclined; it is also sometimes possible to see the intergranular lanes underneath some of the smaller granules (see Figure 1). Nonetheless, the granules are still always blueshifted relative to the intergranular lane components across the stellar disk (see Figure 4).

In addition to the changes in the line shape and position in the four component profiles, there are also variations in their respective filling factors as a function of stellar disk position, shown in Figure 7. From disk center until ∼30° ($\mu \sim 0.87$), all components remain unchanged within 1%, indicating the observable field of view does not change significantly. However, from ∼40°–80° ($\mu \sim 0.67$–0.17)), there is a strong decrease in non-magnetic intergranular lane filling factor and subsequent increase in the granule filling factor. We attribute this to increased granular obstruction of intergranular lanes at these angles where the view is dominated by the top regions of the granular "hills." An analogy for this would be standing on top of one hill and looking straight out across several other hills; from this vantage point, one could only see the very tops of the hills. Again, we see some evidence for the MBP component capturing faculae as the average filling factor remains roughly constant across most of the disk, until it increases very near the limb. The magnetic intergranular lane filling factor is also roughly constant across the disk; this could be because this component captures regions within the intergranular lane where the magnetic flux is strong, but where the flux tube may not be purely radial. If the magnetic flux tubes are not purely radial, then the magnetic flux present may not be sufficient to completely evacuate the tube and the opacities are not greatly affected; hence, these regions are always dark and located within the intergranular lanes (unlike the MBPs). However, the presence of the magnetic flux may be strong enough to alter the opacity in such a way that it counteracts the increased obstruction of the intergranular lanes from the granules. Ergo, a constant magnetic intergranular lane component may mean that the visible non-radial flux tubes are roughly constant across the stellar disk.

4. Parameterized Reconstruction: Across the Stellar Disk

In order to test the robustness of the parameterization scheme at different limb angles, we used the four granulation component profiles to reconstruct the original line profiles output from the MHD simulation. We remind the reader that the original profiles were created by averaging together all Stokes *I* profiles from each pixel in a given snapshot (i.e., they are the same profiles discussed in Section 2). Following the methodology outlined in Paper I, the four component profiles for each limb angle were multiplied by their respective filling factors and summed together to reconstruct the original absorption line profiles output by the simulation. Note that,

because the parameterization is created from time averages, the reconstructed profiles will have no knowledge of the oscillation seen in the original profiles—only the granulation effects will be captured.

4.1. Frequency-power Spectra

Because the oscillations alter both the line shape and center, the original and reconstructed line profiles cannot be compared directly. Moreover, given that the hypothesis from Paper I, regarding how the oscillations only shift the lines and do not alter their shapes, has been shown to be invalid, we should no longer use the average relative error between the original and reconstructed line profiles to evaluate the parameterization accuracy. As an alternative test, we compare the PSDs to the well-known empirical behavior of solar p-modes and granulation. This is particularly powerful, as we can examine the behaviors of both the RVs and the line shape parameters with the same test.

As mentioned in Section 2.1, the cadence of the simulation is close to 30 s, with nearly a third of the snapshots having a cadence closer to ∼15 s, and each snapshot is taken instantaneously, i.e., with zero integration/exposure time. To prevent the non-uniform cadence from impacting the PSD, we linearly interpolate the RVs onto a time grid with a fixed cadence of 30 s and compute frequency-power spectra of these interpolated data; because the granulation and oscillations evolve on timescales of a few minutes, this interpolation should not alter the nature of the data.

Next, we fit the power spectra with the same kind of parametric models used for disk-integrated solar (and stellar) observations, using maximum likelihood estimators to optimize the fit. As the reconstructed RVs should contain solely granulation, we fit their power spectrum with a single "super-Lorentzian" of the form

$$P_{\rm gran} = a_0/(1 + (2\nu/a_1)^{a_2}), \quad (1)$$

where ν is frequency, a_0 is the maximum power spectral density, a_1 calibrates the fall-off of the granulation power with increasing frequency, and a_2 is the exponent of the power-law. Then, as the original RVs contain both granulation and p-modes, we fit the original RVs with the sum of a Lorentzian (for the p-modes) and the aforementioned super-Lorentzian (for the granulation), i.e.,

$$P_{\rm tot} = c_0/(1 + (2(\nu - c_2)/c_1)^2) + P_{\rm gran}, \quad (2)$$

where c_0 is the maximum power spectral density (or height) of the Lorentzian, c_1 is the full-width at half-maximum (FWHM) of the Lorentzian, and c_2 is the central frequency of the Lorentzian.

If the parameterization sufficiently captures the granulation effects, then we can obtain a good fit to the original time series with Equation (2) while holding the super-Lorentzian (Equation (1)) fixed to the values obtained from the reconstructed RV fit; as such, we do exactly that to test this hypothesis.

We perform these fits for data at disk center, as this is where the influence of the p-modes is most pronounced; hence, an adequate fit here should be sufficient to establish that we can model both the p-modes and the granulation in the power spectrum. Because the original MHD simulation captures just a small region on the stellar disk, we cannot compare directly the best-fitting power parameter (a_0) to empirical data. However, we would hope that the characteristic timescale for the granulation ($\tau = 1/(\pi a_1)$) and the power-law exponent (a_2) are both similar to solar observations.

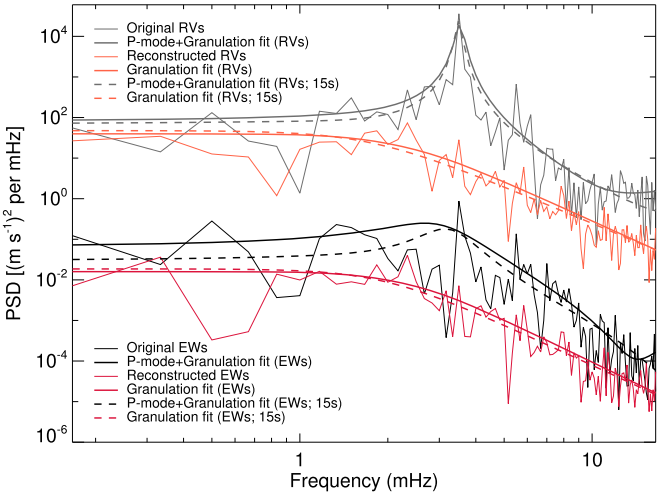

Figure 8. Power spectra, at disk center, of the RVs and equivalent widths from the original and reconstructed line profiles; the equivalent width data has been scaled by a factor of 10^{-3} for viewing ease. Solid lines display an interpolation onto a 30 s cadence and dashed lines for a 15 s cadence; thick lines are the fits to the data (thin lines).

As shown in the top of Figure 8, we are indeed able to obtain good fits for both the reconstructed/granulation RVs and the original/total RVs. Near very high frequencies, the fit to the total RVs starts to turn over toward higher power; to examine whether this behavior was related to the interpolation scheme, we tested both a spline interpolation (rather than linear) and an interpolation onto a 15 s cadence. The spline interpolation produced very similar results (albeit with a slightly worse χ^2/BIC), but the shorter-cadence results (shown as dashed lines in Figure 8) show that the fit continues to fall off in power as expected. Hence, the small upturn in the original RVs' fit near high frequencies is most likely due to the limitations of the interpolation and is not indicative of the MHD simulation. The granulation timescale ($\tau = 214 \pm 23$ s) and exponent ($a_2 = 3.3 \pm 0.2$), derived from the fit of Equation (1) to the reconstructed data, also agree well with known solar observations (206–215 s and 3.6–4.6, respectively) from Michel et al. (2009) and Kallinger et al. (2014). We note also that the p-modes in the original simulation box are centered on a frequency similar to the known empirical solar p-modes, $c_2 = 3.5 \pm 0.06$ mHz ($\nu_{\rm max,\odot} = 3.14$ mHz), from Kallinger et al. (2014).

In addition to the wholesale Doppler shifts induced by the p-modes, they also induce changes in the line shape. To examine if our parameterization captures the correct line shapes, we repeated the above procedure on the equivalent widths (EWs); these are shown alongside the RV results in Figure 8. The best-fitting timescale and exponent for the reconstructed profile EWs agrees very well with the equivalent fit from the RVs ($\tau = 208 \pm 21$ s, $a_2 = 3.5 \pm 0.2$, respectively). Consequently, we find that the reconstructed profile shapes are following the same behavior as their RVs, and therefore we can assert that we also capture the granulation-induced line shape changes with our parameterization. The fit to the original profile EWs is not quite as good as that for the original RVs, but this is likely due to the fact that the

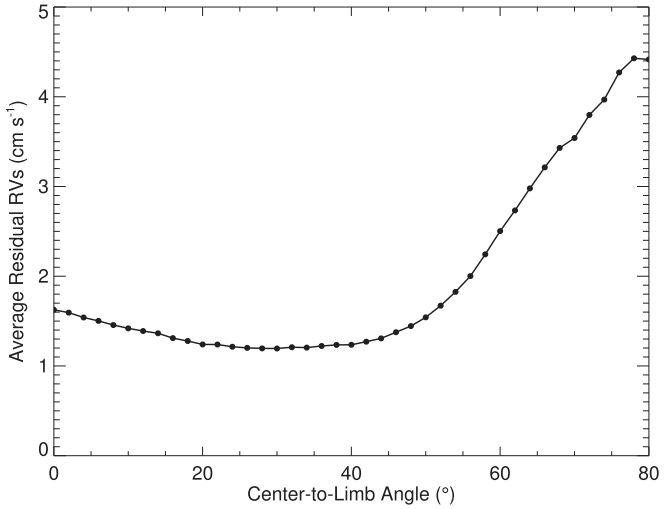

Figure 9. Average residual (original-reconstructed) RVs of the time series as a function of limb angle.

granulation has a larger impact on the profile shapes than the line centers, as compared to the p-modes. Hence, the envelope from the p-modes has less power in the EW PSD and is therefore less well-defined. Additionally, a comparison with the granule filling factor PSD shows the same peak frequency at ∼2.3 mHz that was found in the reconstructed RVs and EWs PSD. A peak at ∼2.3 mHz is also visible in the original PSDs, but at a much lower power than the p-mode frequencies. This adds further evidence that the same frequency content from the granulation parameterization can be seen in the original simulation, but that it is swamped by the large-scale variations induced by the p-modes.

4.2. Residual RVs

To further examine the accuracy of the parameterization in capturing granulation physics, we can still use the hypothesis from Paper I regarding the residual RVs: if the parameterization captures the granulation physics, then a cross-correlation between the original average line profiles and their respective reconstructed profiles should provide the RV shifts from the total oscillation signal. Using a cross-correlation technique here allows the oscillation-induced line shape changes to contribute to the oscillation-induced RV shifts. As such, we can still obtain the original granulation RVs from the MHD simulation by subtracting off the oscillation RVs from the total original RVs. See Paper I for further justifications. Hence, we can examine the residuals between the granulation-induced RVs determined from both the original and reconstructed profiles.

For this analysis, the RVs originate from a cross-correlation with a template (chosen from the reconstructed time-series) at the same center-to-limb angle, as we are interested in the RVs at each limb angle and not relative to disk center; the same template is used with both the original and reconstructed profiles. We found the residuals were always $\leqslant \pm 10\,\mathrm{cm\,s^{-1}}$, until very near the stellar limb, but even at 80° the residuals are still less than $5\,\mathrm{cm\,s^{-1}}$ on average—see Figure 9. The granulation RVs and the residuals between the original and reconstruction for center-to-limb angles 0°, 20°, 40°, 60°, and 80° are presented in Figure 10, which shows how well the parameterization captures the granulation physics at each snapshot.

It is possible that some of the residual RVs could arise from errors in the filling factors due to misidentification of components. Because the four average components are composed of averages from numerous profiles within a single snapshot, as well averages throughout the time series, the average component profiles are likely quite robust, but small changes in the filling factors of a single snapshot could make the reconstruction slightly inconsistent with that particular granulation pattern. If this were the case, it would not be an issue for our parameterization because it would only mean that, in those instances, the reconstruction does not match perfectly the original simulated line profile, and not that the technique produces unrealistic granulation line profiles. Additionally, because the residual RVs are very small, and the reconstructions very accurate, the effect of any misidentification of component filling factors in the overall distribution of filling factors from the time series should be negligible.

It is also possible that some of these residual RVs could originate, not from fault in the logic of the parameterization nor lack of optimal simulation resolution or length, but from random small-scale vortices that originate in the simulations and are averaged out in the creation of the four granulation component profiles. Random small-scale vortices are a byproduct of photospheric magneto-convection and appear in the radiative 3D MHD solar simulations. These small-scale vortices are short-lived and unpredictable. The presence of any such vortices at a particular point in time will introduce small line asymmetries in the average line profile of the corresponding snapshot in the simulations. Given that our four component profiles are created by averaging components in a given category over the time series, it is impossible for these vortices not to be averaged out. However, this is not a problem for our parameterization because its purpose is to simulate model Sun-as-a-star observations of stellar surface granulation, and such disk-integrated observations would also average out the RV variations from these random, short-lived, small-scale vortices (Shelyag et al. 2011).

5. Comparison to Observations

Here, we compare our simulated line profiles with solar observations; for a comparison between different HD/MHD codes, we direct the readers to Beeck et al. (2012).[13] Unfortunately, there are no known observations of the Fe I 6302 Å line that provide both line profile shape and net convective blueshift measurements where the magnetic field is known to be similar to our simulation. As such, we expect some differences when comparing to the literature due to variations in magnetic field strength as compared to the MHD simulation.

5.1. Center-to-limb Line Bisectors

First, we compare line profile shapes by inspecting the line bisectors at various limb angles and comparing them to the solar observations from Cavallini et al. (1985a) and Löhner-Böttcher et al. (2018). Because both of these authors use time averages (either via binned data or long exposures) to smooth out the impact of the p-modes (and increase signal-to-noise), we make this comparison on a line profile created from averaging over the entire simulation time series. Moreover, as

[13] Note that Figures 13 and 14 can be tentatively compared to Figure 18 in Beeck et al. (2013b) and Figure 11 in Beeck et al. (2015b), but one should heed the differences in magnetic field, line choice, and RV calculation.

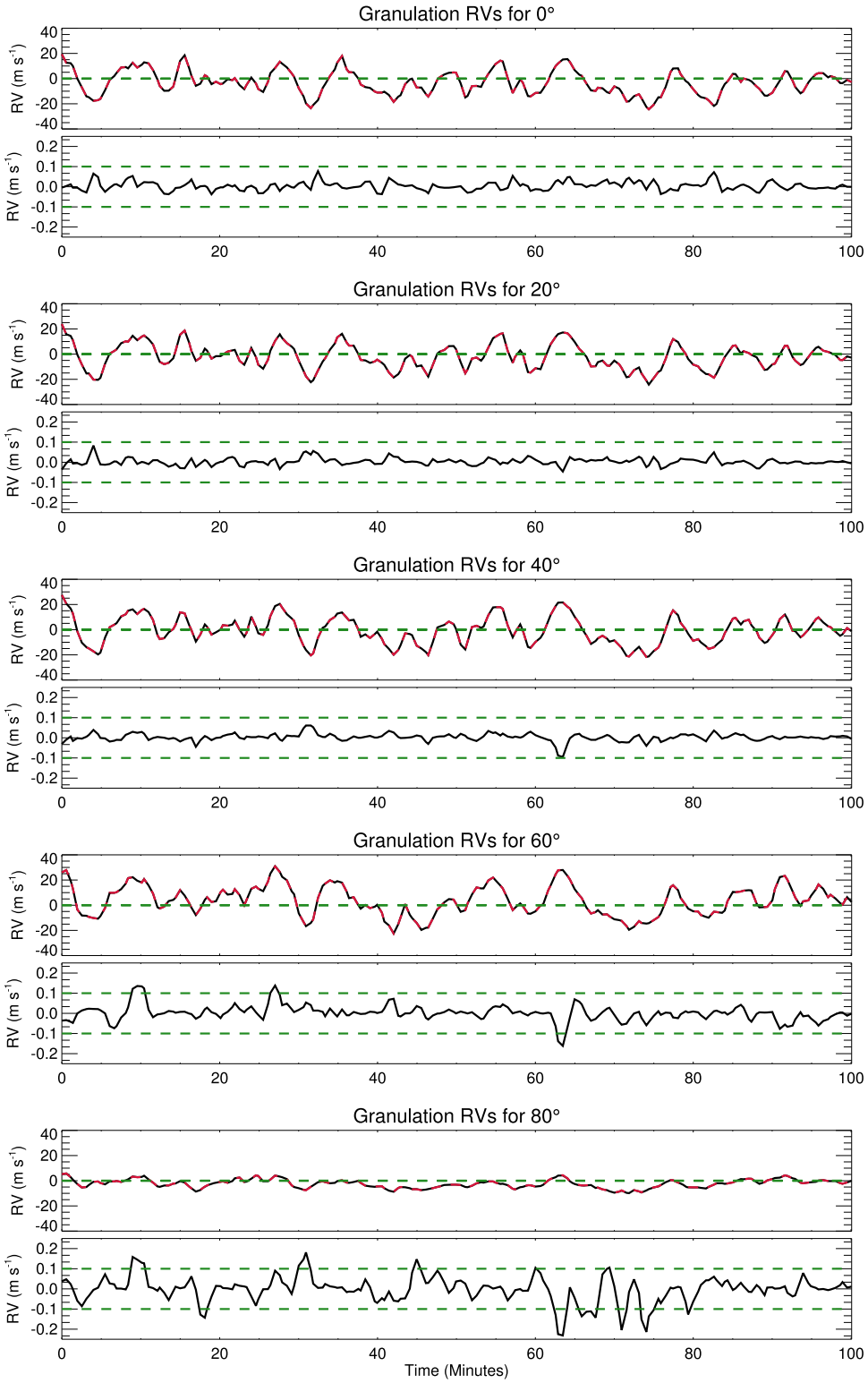

Figure 10. Granulation RVs from the simulation (original-oscillation) are shown in black, and those from the reconstruction are shown in dashed red lines, for various center-to-limb angles; residuals between the two are also shown in black solid lines below. Horizontal dashed lines at ± 10 cm s^{-1} are provided to guide the eye.

we are comparing only the line shape in this instance, we shift the simulated profiles in wavelength to closer examine the bisectors variations (see Figures 12 and 13 for a comparison of net RV). Finally, we convolve our simulated profile with an instrumental profile matching the observations of Cavallini et al. (1985a) (a Gaussian with an FWHM of 40 mÅ); this is particularly important as the symmetric instrumental profile acts to smooth out some of the asymmetries in the underlying Fe I 6302 Å profile. In Figure 11, we can see that our simulated profile shares characteristics of both the observed quiet Sun and facular region profiles. Near disk center, our profiles and those of the observed quiet Sun share a similar blueward slope near

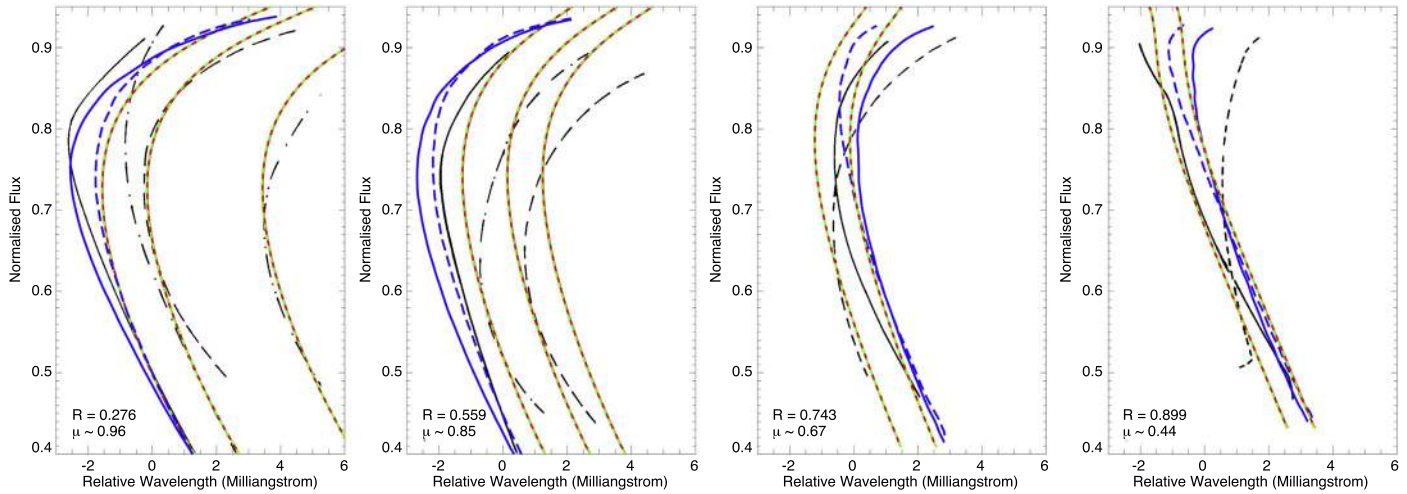

Figure 11. Time-average bisectors from the MHD simulation (red are from the original profiles and dashed green lines are from the reconstruction) for various center-to-limb positions (denoted in units of solar radii and approximate μ), after convolution with an instrumental profile matching Cavallini et al. (1985a). Observations from Cavallini et al. (1985a) are shown in solid black lines for the quiet Sun and dashed/dotted–dashed lines for facular regions; observations from Löhner-Böttcher et al. (2018) for the quiet Sun are shown in blue at μ intervals of 0.1; dashed lines indicate μ lower by 0.1. The simulated profiles and data from Löhner-Böttcher et al. (2018) have been shifted to various positions to ease shape comparison with Cavallini et al. (1985a).

the bottom of the line; at the same position, our simulated profiles are more similar to observed facular region profiles in the redward slope seen in the upper part of the line. Toward the stellar limb, the simulated profile begins to share even more curvature similarities with the quiet Sun observations as compared to the facular regions. This behavior likely indicates that the magnetic field in our simulations is greater than the quiet Sun (as expected), yet smaller than the facular regions observed by Cavallini et al. (1985a). Nonetheless, given the known differences in magnetic field strength, we find good line shape agreement with the observations across the stellar disk.

5.2. Center-to-limb Convective Blueshift

Next, we compare the CLV in the net convective blueshift as a function of limb angle. For the Fe I 6302 Å line, we have CLV measurements for the quiet Sun from Cavallini et al. (1985b) and even higher-precision measurements from Löhner-Böttcher et al. (2018). However, as we know the enhanced magnetic field in our simulation inhibits the convective flows, we anticipate potentially large differences in the CLV.

As such, we have also synthesized a small subsample of Fe I 6302 Å line profiles for a MHD simulation with a net magnetic field of 0 G. This sample includes profiles from six snapshots, separated in time by 20 minutes each, at nine center-to-limb positions, in steps of $\sim$0.1 μ (from 1.0 to 0.1). In this way, this subsample should be sufficient to average out much of the impact from the stellar oscillations, as well as capture the overall center-to-limb behavior. A complete characterization of this simulation is beyond the scope of this paper and will be the subject of future work; its purpose here is simply to investigate the CLV in net convective blueshift as compared to the 200 G simulation presented throughout this work and the empirical quiet Sun observations.

On the other hand, to compare the 200 G simulation with solar observations at different magnetic field strengths, we turn to observations of the Fe I 6173 Å line. Following Haywood et al. (2016) and M. L. Palumbo et al. (2018, in preparation) were able to use AIA data to isolate quiet Sun, faculae network, and plage regions, with increased average magnetic field respectively. The HMI data were then used to extract the local RVs for each region separately. Note that these RVs are expressed relative to the quiet Sun, in order to overcome various instrumental offsets (such as filters drifting over the Fe line); hence, we can only compare the center-to-limb shapes and relative shifts between regions of different magnetic field strength. The Fe I 6173 Å line is quite similar to the Fe I 6302 Å line in terms of physical properties (e.g., line strength, excitation potential, and line broadening parameters), and nearly identical in magnetic sensitivity (i.e., Landé factor). Therefore, it should provide a reasonable comparison. Note that the Fe I 6302 Å line is slightly stronger, with a slightly larger excitation potential (0.58 versus 0.55 and 3.7 versus 2.2 eV, respectively) (Ryabchikova et al. 2015, and references therein).[14]

The calculation of the net convective shift is particularly sensitive to how the RV is measured, as well as the influence of the instrument profiles. The Cavallini et al. (1985b) measurements were determined via the mean of the line bisector up to 70% of the continuum; these measurements were also reported relative to disk center and therefore do not provide an absolute RV scale. Because the Cavallini et al. (1985b) results were reported relative to disk center, we subtracted an offset at 300 m s^{-1} (the expected approximate net convective blueshift of the Sun at disk center) when making our comparison. Löhner-Böttcher et al. (2018) provided measurements calculated both via a mean bisector (this time up to 95% of the continuum) and via a parabolic fit to the line core. Finally, the HMI measurements are reported via a calculation of the first moment. Comparisons to these three techniques are shown in Figures 12–14. For each, we again used the result from a time average over the entire simulation duration,[15] and convolved with the appropriate instrumental profile: a Gaussian with an FWHM of 9, 40, or 76 mÅ, for comparison with Löhner-Böttcher et al. (2018), Cavallini et al. (1985b), or

[14] These values were derived from the VALD database assuming solar properties (http://vald.astro.uu.se).

[15] For the net 0 G simulation, we averaged over the aforementioned six snapshots, separated in time by 20 minutes each.

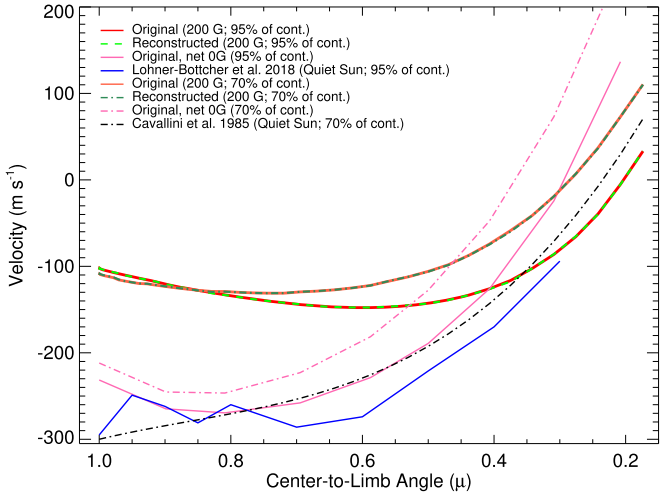

Figure 12. Net RV as a function of limb angle, calculated via the mean bisector up to either 70% or 95% of the continuum, and convolved with the corresponding instrumental profile; thick lines indicate the 200 G simulation.

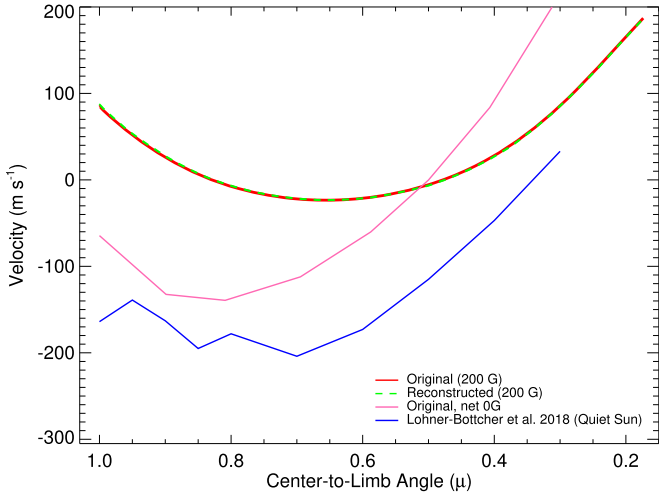

Figure 13. Net RV as a function of limb angle, calculated via a parabolic fit to the bottom of the line profile core. Profiles from the simulations were convolved with the instrumental profile from the LARS spectrograph (thick lines indicate the 200 G simulation).

M. L. Palumbo et al. (2018, in preparation), respectively. We anticipate the RV determined from the line core to be most sensitive to any residual oscillations that may not be completely averaged out in our limited sample of the net 0 G simulation; this is because it is determined from only a small section of the overall line profile (as compared to the mean bisector or first moment). Moreover, because the oscillations become less coherent in phase near the limb (see Figure 3), it may be more difficult to average out the oscillations from randomly selecting snapshots (despite the lower amplitudes near the limb), so the net 0 G simulation may differ from the observations more near the limb. Finally, because the magnetic field dampens the convective motions, it naturally also dampens the induced oscillations; as such, the lower magnetic field strength simulation may require further averaging to bin out the oscillation impact.

It is clear from Figures 12 and 13 that the results from our 200 G MHD simulation are far more redshifted than the quiet Sun observations. The minimum CLV RV, and subsequent steep increase in redshift, also happens closer to the limb in the MHD simulations as compared to the quiet Sun. Both aspects are to be expected because the simulation has a magnetic field strength closer to a facular/plage region than the quiet photosphere, and the enhanced magnetic field retards the plasma flows. This is evidenced by comparisons with the subsample from the net 0 G MHD simulation, as well as the HMI observations of the quiet Sun, network, and plage regions. In Figures 12–14, we see in each instance that the net 0 G simulation matches much more closely the empirical observations from Cavallini et al. (1985b), Löhner-Böttcher et al. (2018), and M. L. Palumbo et al. (2018, in preparation), where the differences can be attributed to small differences in net magnetic field strength and/or the impact of non-perfect smoothing over the stellar oscillations (see Figure 3 for the impact of the oscillations on the center-to-limb behavior). In particular, we highlight that the larger differences between the 0 G simulation and observations seen in Figure 13 are in line with what we expect due to contamination from residual oscillation signatures.

Moreover, from the HMI observations in Figure 14, we can observe the impact of increasing magnetic field by comparing the quiet photosphere to the more magnetic facular network

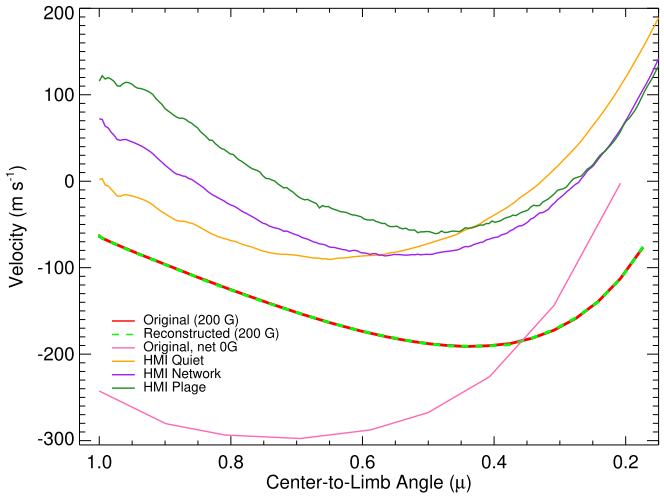

Figure 14. Net RV as a function of limb angle, calculated via the first moment. Profiles from the simulation were convolved with the instrumental profile of HMI (thick lines indicate the 200 G simulation). The Fe I 6173 Å HMI observations are separated into contributions from the quiet photosphere, facular network, and plage regions (with increasing magnetic field respectively), and are relative to the quiet Sun.

regions and the even more magnetic plage regions. In doing so, we see that an increase in magnetic field increases the net redshift, as well as the initial gradient in the CLV; it also pushes the minimum CLV toward the solar limb. This same general behavior from the HMI observations can be seen when comparing the subsample of net 0 G simulation to the full 200 G simulation. There is some variance between simulation and observation, in the relative shift between the "quiet" and more "active" regions, but we attribute this largely to differences in the net magnetic field strength and configuration. We note that the main distinction between the simulated 6302 Å line and observed 6173 Å line behavior is the gradient in the initial blueshift; however, this could be due to slight variations in the formation heights of the two lines. Overall, the magnitude and behavior of the CLV in both line profile shape and net convective blueshift match the observations well, given

the known differences in magnetic field strength (and also line properties in regards to HMI).

6. Concluding Remarks

Throughout this paper, we have extended the multi-component parameterization of magneto-convection from disk center (Paper I) toward the stellar limb. Away from disk center, contributions from plasma flows orthogonal to the granule tops become significant and the geometry of the granular hills and intergranular lane valleys play a vital role in the resultant line profile asymmetries/shifts. In particular, we have examined the CLV in net RV, and broken down the increase in redshift toward the limb into the individual granulation component contributions. We found that the granule and non-magnetic intergranular lane line profiles decreased in line depth and increased in line width toward the limb, whereas the magnetic components initially increased in line depth and decreased in line width as they were viewed toward the limb and subsequently through areas of lower magnetic flux. Near the limb, granules continued to redshift and the intergranular lane components continued to blueshift relative to disk center—though the granules were still always blueshifted relative to the intergranular lane components. Moreover, the granule filling factor continued to increase toward the limb as the granules obstructed the intergranular lane components. The MBP component likely captures the hot granular walls (faculae) off disk center, which prevents its continuum intensity from falling off until closer to $\sim 50^{\circ}$. The result of all this behavior is due to the relationships between the visible plasma flows and the corrugated nature of the granulation.

We also compared the results from our simulation to various empirical observations of the Sun. Given the differences in magnetic field strength, we found good center-to-limb agreement in the bisector shape, the net RV, the p-mode amplitude/power, and behavior of the PSD for both the RVs and equivalent width. It was crucial to examine the line shape behavior, as we found that both the p-modes and the granulation change the line shape. We also determined that our parameterization can recreate the granulation RV shifts found in the MHD simulation to better than $10\,\mathrm{cm\,s^{-1}}$ across the stellar disk. Hence, we are confident that our granulation parameterization captures both the line shape and RV shifts indicative of solar surface convective flows. As such, in a forthcoming paper, we will use this parameterization and the probability distributions of the filling factors from the time-series herein to create new granulation profiles representative of those that would be produced through the more computationally intensive radiative 3D MHD simulations. These new granulation line profiles will then be used to create Sun-as-a-star model observations to examine the granulation induced line shape changes and their relationship with the induced RV shifts. Later, we can extend this work to different magnetic field strengths and line profiles with different physical properties. Ultimately, we aim to determine the optimum techniques to remove granulation (and potentially oscillation) induced line asymmetries and RV shifts from exoplanet observations. This work is vital to overcome the barriers of astrophysical noise and detect true Earth analogues in the future.

The authors would like to thank S. Sulis for useful discussions regarding colored noise and periodograms, and J. Löhner-Böttcher for sharing results from the LARS spectrograph. The authors also thank the anonymous referee for useful comments, which improved the clarity of this manuscript. H.M.C. acknowledges the financial support of the National Centre for Competence in Research PlanetS supported by the Swiss National Science Foundation (SNSF); S.S., H.M.C, and C.A.W acknowledge support from the Leverhulme Trust. W.J.C., G.R.D., and C.A.W. acknowledge support from the UK Science and Technology Facilities Council (STFC), including grants ST/I001123/1 and ST/P000312/1. Funding for the Stellar Astrophysics Centre is provided by The Danish National Research Foundation (Grant agreement no.: DNRF106). S.H.S. was supported by NASA Heliophysics LWS grant NNX16AB79G, and M.L.P. was supported by the NSF-REU solar physics program at SAO, grant number AGS-1560313. Some of this work was performed under contract with the California Institute of Technology (Caltech)/Jet Propulsion Laboratory (JPL) funded by NASA through the Sagan Fellowship Program executed by the NASA Exoplanet Science Institute (R.D.H.). This work used the DiRAC Data Centric system at Durham University, operated by the Institute for Computational Cosmology on behalf of the STFC DiRAC HPC Facility; DiRAC is part of the National E-Infrastructure. This research has made use of NASA's Astrophysics Data System Bibliographic Services, as well as the VALD database operated at Uppsala University, the Institute of Astronomy RAS in Moscow, and the University of Vienna.

Software: MURaM (Vögler et al. 2005; Shelyag & Przybylski 2014; Shelyag 2015); OPAL (Rogers et al. 1996; Rogers & Nayfonov 2002); NICOLE (Socas-Navarro 2015; Socas-Navarro et al. 2015).

ORCID iDs

H. M. Cegla https://orcid.org/0000-0001-8934-7315
S. Shelyag https://orcid.org/0000-0002-6436-9347
W. J. Chaplin https://orcid.org/0000-0002-5714-8618
G. R. Davies https://orcid.org/0000-0002-4290-7351
M. Mathioudakis https://orcid.org/0000-0002-7725-6296
M. L. Palumbo III https://orcid.org/0000-0002-4677-8796
R. D. Haywood https://orcid.org/0000-0001-9140-3574

References

Asplund, M., Nordlund, Å., Trampedach, R., Allende Prieto, C., & Stein, R. F. 2000, A&A, 359, 729
Balthasar, H. 1985, SoPh, 99, 31
Beeck, B., Cameron, R. H., Reiners, A., & Schüssler, M. 2013a, A&A, 558, A48
Beeck, B., Cameron, R. H., Reiners, A., & Schüssler, M. 2013b, A&A, 558, A49
Beeck, B., Collet, R., Steffen, M., et al. 2012, A&A, 539, A121
Beeck, B., Schüssler, M., Cameron, R. H., & Reiners, A. 2015a, A&A, 581, A42
Beeck, B., Schüssler, M., Cameron, R. H., & Reiners, A. 2015b, A&A, 581, A43
Cavallini, F., Ceppatelli, G., & Righini, A. 1985a, A&A, 143, 116
Cavallini, F., Ceppatelli, G., & Righini, A. 1985b, A&A, 150, 256
Cegla, H. M., Shelyag, S., Watson, C. A., & Mathioudakis, M. 2013, ApJ, 763, 95
Chaplin, W. J., Cegla, H. M., Watson, C. A., & Davies, G. R. 2018, AJ, submitted
Christensen-Dalsgaard, J. 2002, RvMP, 74, 1073
Dravins, D. 1982, ARA&A, 20, 61
Dravins, D. 2008, A&A, 492, 199
Dumusque, X., Udry, S., Lovis, C., Santos, N. C., & Monteiro, M. J. P. F. G. 2011, A&A, 525, A140
Gray, D. F. 2005, The Observation and Analysis of Stellar Photospheres (Cambridge: Cambridge Univ. Press)

Haywood, R. D., Collier Cameron, A., Unruh, Y. C., et al. 2016, MNRAS, 457, 3637
Kallinger, T., De Ridder, J., Hekker, S., et al. 2014, A&A, 570, A41
Löhner-Böttcher, J., Schmidt, W., Stief, F., Steinmetz, T., & Holzwarth, R. 2018, A&A, 611, A4
Meunier, N., Lagrange, A.-M., Borgniet, S., & Rieutord, M. 2015, A&A, 583, A118
Michel, E., Samadi, R., Baudin, F., et al. 2009, A&A, 495, 979
Robertson, P., Roy, A., & Mahadevan, S. 2015, ApJL, 805, L22
Rogers, F. J., & Nayfonov, A. 2002, ApJ, 576, 1064
Rogers, F. J., Swenson, F. J., & Iglesias, C. A. 1996, ApJ, 456, 902
Ryabchikova, T., Piskunov, N., Kurucz, R. L., et al. 2015, PhyS, 90, 054005
Saar, S. H., & Donahue, R. A. 1997, ApJ, 485, 319
Schmidt, W., Stix, M., & Wöhl, H. 1999, A&A, 346, 633
Schrijver, C. J., & Zwaan, C. 2000, Solar and Stellar Magnetic Activity (Cambridge: Cambridge Univ. Press)
Shelyag, S. 2015, ApJ, 801, 46
Shelyag, S., Keys, P., Mathioudakis, M., & Keenan, F. P. 2011, A&A, 526, A5
Shelyag, S., & Przybylski, D. 2014, PASJ, 66, S9
Socas-Navarro, H. 2015, NICOLE: NLTE Stokes Synthesis/Inversion Code, Astrophysics Source Code Library, ascl:1508.002
Socas-Navarro, H., de la Cruz Rodríguez, J., Asensio Ramos, A., Trujillo Bueno, J., & Ruiz Cobo, B. 2015, A&A, 577, A7
Stein, R. F. 2012, LRSP, 9, 4
Vögler, A., Shelyag, S., Schüssler, M., et al. 2005, A&A, 429, 335